IV International Conference on Simulation for Additive Manufacturing
Sim-AM 2023
E. Rank and S. Kollmannsberger (Eds)

INCREMENTAL VISCOELASTICITY FOR 3D CONCRETE PRINTING: FINITE STRAIN MODELING AND PARAMETRIC STUDIES

B. NEDJAR*, Z. AWADA† AND J.M. TORRENTI‡

*Université Gustave Eiffel, MAST-EMGCU,
5 Boulevard Descartes, 77454 Marne-la-Vallée cedex 2, France
e-mail: boumediene.nedjar@univ-eiffel.fr

† Sorbonne Université, Institut Jean Le Rond ∂'Alembert, CNRS UMR 7190,
4 Place Jussieu, 75005 Paris, France
e-mail: zeinab.awada@sorbonne-universite.fr

‡ Université Gustave Eiffel, UMR MCD-Cerema,
5 Boulevard Descartes, 77454 Marne-la-Vallée cedex 2, France
e-mail: jean-michel.torrenti@univ-eiffel.fr

Key words: Additive Manufacturing (AM), 3D Concrete Printing (3DCP), Large deformations, Computational modeling, Parametric studies

Abstract. Within a 3D concrete printing process, concrete is still fresh and possible collapse may occur due to its own weight and lack of formwork. On the other hand, the mechanical characteristics of the material are continuously evolving due to hydration during curing. Within a predictive theory, the constitutive relation of the early age concrete is to be defined in rate form. In this contribution, and due to the soft nature of the problem at hand, a finite strain incremental viscoelastic modeling is adopted. A generalized Maxwell rheological model is used together with a Saint-Venant-like incremental elasticity. A parametric study is conducted on simulated slump-tests to highlight the abilities of the present framework. Clearly, the early age rheology and mechanical properties have a great impact on the buildability of the fresh concrete. A set of simulations is then given for the purpose of demonstration.

1 INTRODUCTION

Additive manufacturing is nowadays gaining more and more interest, e.g. [9, 8, 3, 22]. It is for instance mostly based on a layer-by-layer extrusion technique. In civil engineering, the still fresh concrete must be able to retain its shape due to the lack of confining formworks. Its buildability is largely influenced by its early age rheology, e.g. [7, 10, 15]. Indeed, under certain conditions, the initially low mechanical properties can lead to possible collapse during the printing process. On another hand, with evolving mechanical properties due to hydration, the stress-strain constitutive relation is of hypo-elastic type (incremental elasticity), a result that has been stated by an abundant literature on early-age concrete, e.g. [2, 4, 5]. It is then mandatory to take this fact into account within a predictive theory involving geometrical nonlinearities.

In recent literature, different numerical models have been proposed, for example as in [18, 20, 12, 13, 17, 16]. Herein, use is made of the one developed in [13, 14]. For the incremental formulation, an adequate kinematic choice is adopted. Use is made of a multiplicative decomposition of the current deformation gradient into its known part at an earlier time and a relative deformation gradient with respect to the configuration at that time. This gives rise to an intermediate configuration on which incremental constitutive relations for the stress state and evolution equations for early-age creep can be well defined. As a Lagrangian formulation is adopted for the mechanical equilibrium, the constitutive equations are pull-back from the known intermediate configuration toward the reference configuration. The above kinematics is well suited for this transport procedure.

Motivated by the generalized Maxwell model, we use an additive decomposition of the incremental stress that is based on a Saint-Venant-like model together with an incremental overstress. In this contribution, we show the effectiveness of the proposed framework. In particular, to capture the influence of the printing speed on the occurrence of structural buckling instabilities. This could certainly help the optimization of the printing process through simulations that could limit the number of costly real experiments. Early age rheology has a strong influence on the buildability and performance. A parametric study on simulated slump-like tests is presented that could introduce, in future works, a possible method to help identifying the material parameters relative to the early-age creep.

2 BASIC EQUATIONS

As the finite strain range is assumed, the equilibrium equation is equivalently written in terms of the second Piola-Kirchhoff stress tensor $\boldsymbol{S}$ as:

$$\int_{\mathcal{B}_0} \boldsymbol{S} : \boldsymbol{F}^T \nabla_{\boldsymbol{X}}(\delta\boldsymbol{\varphi}) \, \mathrm{d}V = \int_{\mathcal{B}_0} \rho_0 \bar{\boldsymbol{b}}.\delta\boldsymbol{\varphi} \, \mathrm{d}V \tag{1}$$

that holds for any admissible variation $\delta\boldsymbol{\varphi}$ of the deformation $\boldsymbol{\varphi}$, $\boldsymbol{F} = \nabla_{\boldsymbol{X}}\boldsymbol{\varphi}$ is the deformation gradient where $\nabla_{\boldsymbol{X}}(\centerdot)$ is the material gradient operator, ρ_0 is the initial density, and $\rho_0\bar{\boldsymbol{b}}$ defines the body force vector due to the self-weight. Here and in all what follows, the double dot symbol $'\!:\!'$ is used for double contraction, i.e. for any second-order tensors $\boldsymbol{A}$ and $\boldsymbol{B}$, one has $\boldsymbol{A} : \boldsymbol{B} = \mathrm{tr}[\boldsymbol{A}\boldsymbol{B}^T] = A_{ij}B_{ij}$ where summation on repeated indices is assumed.

Unlike classical constitutive relations where stresses are directly linked to strain measures, here the stress is restricted to be defined in incremental form. Within a typical time interval $[t_n, t_{n+1}]$, we write:

$$\boldsymbol{S} = \boldsymbol{S}_n + \Delta\boldsymbol{S} \tag{2}$$

where $\boldsymbol{S}_n$ is the *known* stress tensor at time $t = t_n$, and $\Delta\boldsymbol{S}$ is the second Piola-Kirchhoff stress tensor *increment* at the current time $t \in [t_n, t_{n+1}]$. With (2) into (1), the balance equation to be solved is:

$$\int_{\mathcal{B}_0} (\boldsymbol{S}_n + \Delta\boldsymbol{S}) : \boldsymbol{F}^T \nabla_{\boldsymbol{X}}(\delta\boldsymbol{\varphi}) \, \mathrm{d}V = \int_{\mathcal{B}_0} \rho_0 \bar{\boldsymbol{b}}.\delta\boldsymbol{\varphi} \, \mathrm{d}V \tag{3}$$

This equation is valid for all classes of incremental constitutive relations through the definition of model-dependent stress increment $\Delta \boldsymbol{S}$ including, for instance, creep. Precisely for this latter, we use in this work a generalized Maxwell model where the stress is additively split as

$$\boldsymbol{S} = \boldsymbol{S}^{\infty} + \boldsymbol{Q} \tag{4}$$

where $\boldsymbol{S}^{\infty}$ is the equilibrium part, and the internal tensor variable $\boldsymbol{Q}$ may be interpreted as a non-equilibrium over-stress [6, 19, 13]. Eq. (2) becomes;

$$\boldsymbol{S} = \underbrace{\boldsymbol{S}^{\infty}_{n} + \boldsymbol{Q}_{n}}_{=\boldsymbol{S}_{n}} + \underbrace{\Delta \boldsymbol{S}^{\infty} + \Delta \boldsymbol{Q}}_{=\Delta \boldsymbol{S}} \tag{5}$$

We now have to define an incremental constitutive relation for the equilibrium part $\Delta \boldsymbol{S}^{\infty}$, and hence the update of $\boldsymbol{S}_{\infty}$. Here we postulate the following Saint-Venant-like relation, see [12] for more details:

$$\Delta \boldsymbol{S}^{\infty} \;=\; \lambda_{\infty}(t)\; [(\boldsymbol{E} - \boldsymbol{E}_{n}) : \boldsymbol{1}]\, \boldsymbol{1} \;+\; 2\mu_{\infty}(t) \Big(\boldsymbol{E} - \boldsymbol{E}_{n} \Big) \tag{6}$$

where $\boldsymbol{E}$ is the *current* Green-Lagrange strain tensor, $\boldsymbol{E}_{n}$ is its known value at time $t = t_{n}$. Here and in all what follows, $\boldsymbol{1}$ is the second-order identity tensor of components δ_{ij}, i.e. the Kronecker delta.

The time-dependent parameters $\lambda_{\infty}(t)$ and $\mu_{\infty}(t)$ are Lamé-like coefficients within the asymptotic infinitesimal limit. They are related to the time-dependent Young's modulus $E_{\infty}(t)$ and Poisson's ratio $\nu(t)$ of the equilibrium part as:

$$\lambda_{\infty}(t) = \frac{\nu(t)\, E_{\infty}(t)}{(1+\nu(t))(1-2\nu(t))} \qquad\qquad \mu_{\infty}(t) = \frac{E_{\infty}(t)}{2(1+\nu(t))} \tag{7}$$

In addition, we need to specify an evolution equation for the internal variable $\boldsymbol{Q}$. This is motivated by the generalized Maxwell model. Still within the time interval $[t_{n}, t_{n+1}]$, we have shown in [13] that the discrete update is given by:

$$\boldsymbol{Q}_{n+1} \;=\; e^{-\omega \Delta t}\, \boldsymbol{Q}_{n} \;+\; f\, \frac{1 - e^{-\omega \Delta t}}{\omega \Delta t}\, \Delta \boldsymbol{S}^{\infty} \tag{8}$$

where $\Delta t = t_{n+1} - t_{n}$, and $\boldsymbol{Q}_{n}$ is the known (stored) value of $\boldsymbol{Q}$ at time t_{n}, while ΔS^{∞} has just been evaluated in Eq. (6). Here the adimensional parameter f is a scaling factor of the overstress contribution, chosen to be constant for the sake of simplicity. The quantity ω is given by,

$$\omega \;=\; \frac{\dot{E}_{\infty}}{E_{\infty}} + \frac{1}{\tau} \tag{9}$$

in terms of the characteristic time τ and the rate of change of the early-age Young modulus $E_{\infty}(t)$.

Once $\boldsymbol{Q}_{n+1}$ is updated with the help of Eq. (8), the difference $\Delta \boldsymbol{Q} = \boldsymbol{Q}_{n+1} - \boldsymbol{Q}_{n}$ is to be evaluated and then replaced into Eq. (5) for the (total) stress increment $\Delta \boldsymbol{S}$. This latter is used in the balance equation (3) to be solved at the global level.

In summary, the mechanical parameters needed to identify the behavior of the early-age concrete are:

1. $E_\infty(t)$, the time-dependent Young's modulus function;
2. $\nu(t)$, the time-dependent Poisson's ratio. This latter will be considered constant in the simulations below due to the lack of informations;
3. f, the adimensional scaling over-stress factor;
4. τ, the early-age characteristic time.

3 NUMERICAL IMPLEMENTATION AND FINITE ELEMENT OVERVIEW

In a finite element context, the interpolations of the reference geometry and displacements are completely standard. Over a typical finite element $\mathcal{B}_e$ they take the form,

$$\boldsymbol{X}_e(\boldsymbol{\zeta}) = \sum_{A=1}^{n^e_{\text{node}}} N^A(\boldsymbol{\zeta})\boldsymbol{X}^e_A \qquad\qquad \boldsymbol{u}_e(\boldsymbol{\zeta}) = \sum_{A=1}^{n^e_{\text{node}}} N^A(\boldsymbol{\zeta})\boldsymbol{u}^e_A \tag{10}$$

where $\boldsymbol{X}_A \in \mathbb{R}^{n_{\text{dim}}}$, $\boldsymbol{u}_A \in \mathbb{R}^{n_{\text{dim}}}$ denote the reference position and the displacement vector associated with the element node A, $n_{\text{dim}} = 2$ or 3 is the space dimension, n^e_{node} is the node number within the element, and $N^A(\boldsymbol{\zeta})$ are the classical isoparametric shape functions. The interpolation of the deformation gradient then takes the form,

$$\boldsymbol{F}_e(\boldsymbol{\zeta}) = \sum_{A=1}^{n^e_{\text{node}}} (\boldsymbol{X}^e_A + \boldsymbol{u}^e_A) \otimes \nabla_{\boldsymbol{X}}[N^A] \qquad \text{with} \quad \nabla_{\boldsymbol{X}}[N^A] = \boldsymbol{J}(\boldsymbol{\zeta})^{-T}\nabla_{\boldsymbol{\zeta}}[N^A] \tag{11}$$

where $\nabla_{\boldsymbol{\zeta}}[\centerdot]$ is the gradient relative to the isoparametric coordinates, and $\boldsymbol{J}(\boldsymbol{\zeta}) = \partial\boldsymbol{X}_e(\boldsymbol{\zeta})/\partial\boldsymbol{\zeta}$ denotes the Jacobian of the isoparametric map $\boldsymbol{\zeta} \to \boldsymbol{X}$.

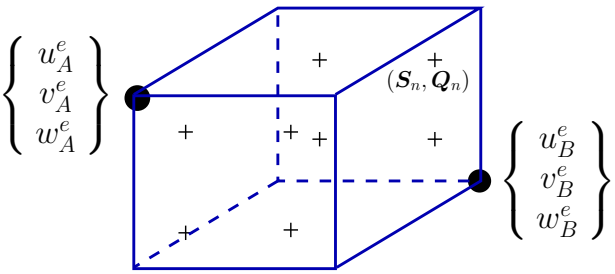

Figure 1: Typical finite element with nodal *dof*s and integration points where the stress and the internal variable are stored.

Equation $(11)_1$ is used for the discrete variation and increment of the Green-Lagrange strain tensor. For instance for the latter:

$$\Delta\boldsymbol{E} = \frac{1}{2}\sum_{A=1}^{n^e_{\text{node}}} \Big[\boldsymbol{F}_e^T(\Delta\boldsymbol{u}^e_A \otimes \nabla_{\boldsymbol{X}} N^A) + (\nabla_{\boldsymbol{X}} N^A \otimes \Delta\boldsymbol{u}^e_A)\boldsymbol{F}_e\Big] = \sum_{A=1}^{n^e_{\text{node}}} \mathbb{B}[N^A]\,\Delta\boldsymbol{u}^e_A \tag{12}$$

in terms of the nodal displacement increments $\Delta \boldsymbol{u}_A^e$, and where $\mathbb{B}[\bullet]$ is the discrete Green-Lagrange strain operator. The element contribution to the global tangent stiffness matrix and residual associated with the element nodes are written from (3) as,

$$\begin{aligned} \mathbf{K}_e^{AB} &= \int_{\mathcal{B}_e} \mathbb{B}^T[N^A]\, \overline{\boldsymbol{\Xi}}^{\text{algo}}\, \mathbb{B}[N^B]\, \mathrm{d}V_e + \left\{ \int_{\mathcal{B}_e} (\nabla_{\boldsymbol{X}}[N^A])^T (\boldsymbol{S}_n + \Delta\overline{\boldsymbol{S}})\, \nabla_{\boldsymbol{X}}[N^B]\, \mathrm{d}V_e \right\} \boldsymbol{I}_{n_{\text{dim}}} \\ \mathbf{R}_e^A &= \int_{\mathcal{B}_e} \Big[N^A \rho_0 \bar{\boldsymbol{b}} - \mathbb{B}^T[N^A]\, (\boldsymbol{S}_n + \Delta\overline{\boldsymbol{S}}) \Big]\, \mathrm{d}V_e \end{aligned} \tag{13}$$

for $A, B = 1, \dots n^e_{\text{node}}$, see Fig. 1 for an illustration, and $\boldsymbol{I}_{n_{\text{dim}}}$ is the $n_{\text{dim}} \times n_{\text{dim}}$ identity matrix, and $\overline{\boldsymbol{\Xi}}^{\text{algo}}$ is the fourth-order algorithmic tangent modulus.

At the end of the global resolution, the stress field $\boldsymbol{S}_{n+1}$ and the updated stress-like internal variable $\boldsymbol{Q}_{n+1}$ via the evolution equation (8). They are stored at the integration points level during the whole iterative process, see again Fig. 1, a procedure that is similar to the ones classically used in modelings involving internal variables, e.g. [1, 11] for example.

Last but not least, $\overline{\boldsymbol{\Xi}}^{\text{algo}}$ is deduced from (6) together with the algorithmic update (8):

$$\overline{\boldsymbol{\Xi}}^{\text{algo}} \equiv \frac{\partial\, \Delta \boldsymbol{S}}{\partial\, \Delta \boldsymbol{E}} = \Big(1 \,+\, f\, \frac{1 - e^{-\omega \Delta t}}{\omega \Delta t} \Big)\, \overline{\boldsymbol{\Xi}}^{\infty} \qquad \text{with} \quad \overline{\boldsymbol{\Xi}}^{\infty} = \lambda_\infty(t) \mathbf{1} \otimes \mathbf{1} + 2\mu_\infty(t) \boldsymbol{I} \tag{14}$$

where $\boldsymbol{I}$ is the fourth-order identity tensor, i.e. such that $\boldsymbol{I} : \boldsymbol{A} = \boldsymbol{A}$ for any second-order tensor $\boldsymbol{A}$, and of components $I_{ijkl} = \frac{1}{2}(\delta_{ik}\delta_{jl} + \delta_{il}\delta_{jk})$.

4 PARAMETRIC STUDIES AND NUMERICAL SIMULATIONS

It is of major importance to correctly identify the mechanical parameters of the early-age concrete. For a given formulation of a concrete, this could certainly help optimizing the printing process via numerical tools. In the absence of experimental data, we give in this section a set of simulations to show the capacities of the present theoretical and numerical framework.

4.1 A parametric study for the creep at early-age

It is obvious that different concrete mixes would slump differently. It would then be advantageous to be able to numerically simulate such a very popular test. Let us consider a classical cone of 300 mm height, with a diameter of 200 mm at the bottom, and an upper diameter of 100 mm, see Fig. 2(a). The simulations are performed as an axisymmetric problem. To fix the ideas, we consider the following very low early-age mechanical parameters, basically, an almost liquid concrete:

$$E_\infty(t) = 0.0025 + 0.001t\,[\text{MPa}] \qquad \nu = 0.3 \qquad f = 2 \qquad \tau = 0.06\,\text{min} \tag{15}$$

where the Poisson's ratio is kept constant for the sake of simplicity. The time t is expressed in minutes. For the self-weight, a density $\rho_0 = 2070\,\text{kg/m}^3$ is used.

In the simulations below, a frictional contact is accounted for with the bottom horizontal surface, see for example [21]. Fig. 2(b) shows the deformed configuration when the cone is almost instantly removed. Afterwards, the deformation still evolves due to the early-age creep as illustrated in Fig. 2(c), see also [13].

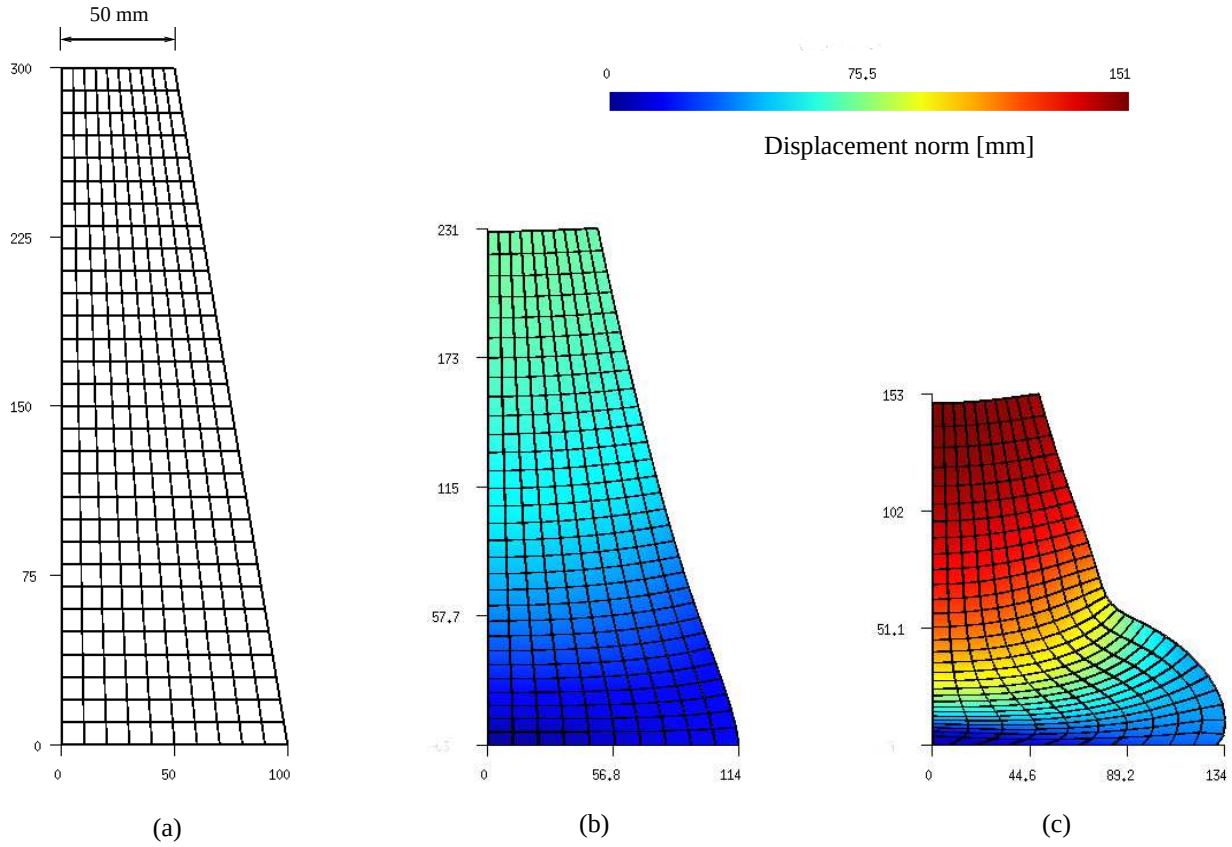

Figure 2: Slump-test simulation: (a) Axisymmetric geometry and finite element mesh, (b) instantaneous slump, (c) delayed slump due to early-age creep. The parameters are those given in (15).

Now to show the influence of the early-age creep paramaters f and τ, two studies are conducted by keeping unchanged the time-dependent Young's modulus $E_\infty(t)$ and Poisson's ratio ν as given in (15). In Fig. 3, for an over-stress scaling factor fixed to $f = 2$, we show the influence of the characteristic time τ, ranging here from few seconds to 3 minutes. The different curves illustrate the evolution of the displacement vs time of the upper center node. One can notice the influence of the characteristic time on the kinetics of the delayed deformations.

In Fig. 4, we show the influence of the over-stress scaling factor f, with this time the characteristic time fixed to $\tau = 1\,\text{min}$. One can notice the influence of the factor f on the early age stiffness of the material, while the kinetics is almost identical for all the simulations.

In all curves of Figs. 3 and 4, the first jump corresponds to the instantaneous withdrawal of the cone, then, delayed displacement takes place depending on the early-age viscosity characteristics.

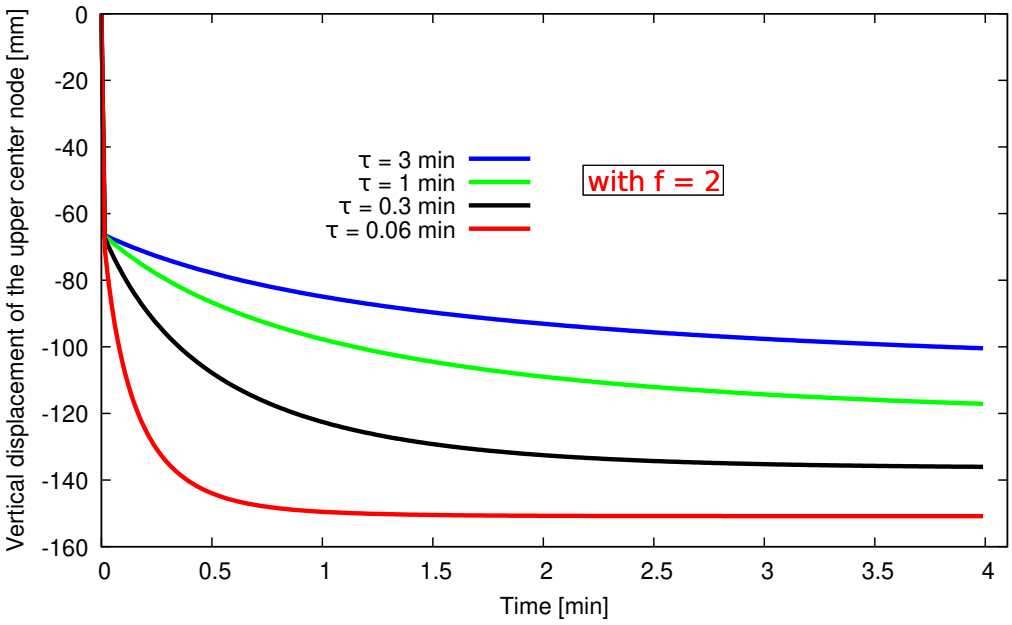

Figure 3: Slump-test simulations: Vertical displacement of the upper center node for different values of the characteristic time τ. Here $f = 2$ is fixed.

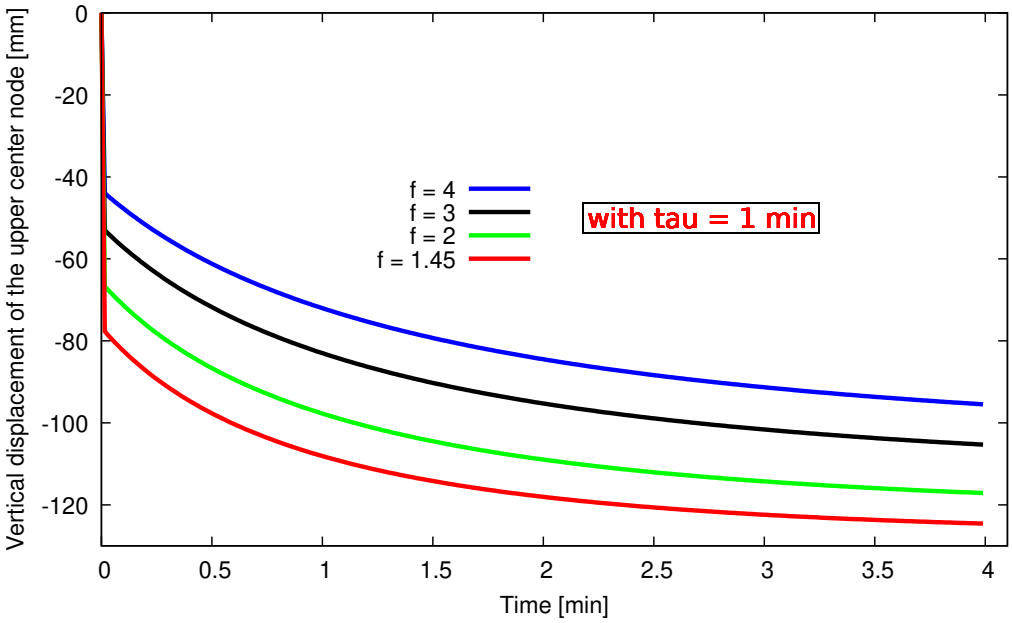

Figure 4: Slump-test simulations: Vertical displacement of the upper center node for different values of the over-stress scaling factor f. Here $\tau = 1\,\text{min}$ is fixed.

4.2 A closed wall printed with thick layers

We consider the closed wall described in Fig. 5, a variant of a similar example already discussed in [14]. It is manufactured layer-by-layer, each layer with cross-section dimensions of

45 mm width and, this time, with thicker layers of 30 mm height. With the model described in Section 2, we consider low mechanical properties so as to trigger structural buckling:

$$E_\infty(t) = 0.04 + 0.02t\,[\text{MPa}] \qquad \nu = 0.3 \qquad f = 0.5 \qquad \tau = 5\,\text{min} \tag{16}$$

where the time t is here again expressed in minutes.

During the simulations, the Young's modulus E_∞ is updated for each layer within the time increments. It enters into the definition of the Lamé-like coefficients of Eq. (7). For the self-weight loading, we consider the density $\rho_0 = 2020\,\text{kg/m}^3$. For symmetry reasons, only one-fourth wall is considered for the finite element discretization with adequate boundary conditions.

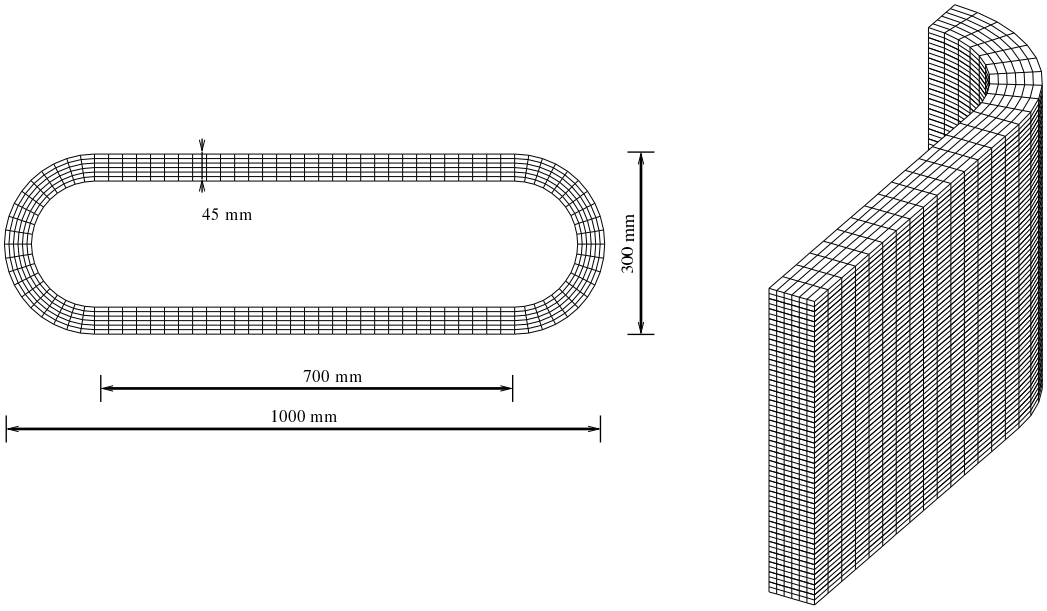

Figure 5: Geometry of the closed wall (top view), and finite element discretization of 1/4-wall up to 10 layers of 30 mm thickness each.

At a printing speed of 2 minutes per layer, Fig. 6 shows the deformed configuration till the end of the simulation with 10 layers. Here the wall remains almost straight until the end of the computation.

Now for a four times faster printing simulation, at a speed of 0.5 minutes per layer, the wall starts to visibly deviate at the 8th layer. The computed wall after 10 layers shows a very large deformation meaning collapse in bending more. For illustrative purposes, Fig. 7 shows the sequence from the 7 layers wall until the end of the simulation with 10 layers.

This example shows that the present modeling framework is able to capture the influence of the printing speed on the stability of the printed structures. It is obvious that the precise knowledge of the model parameters of the fresh concrete and its rheology is of great importance for the whole process.

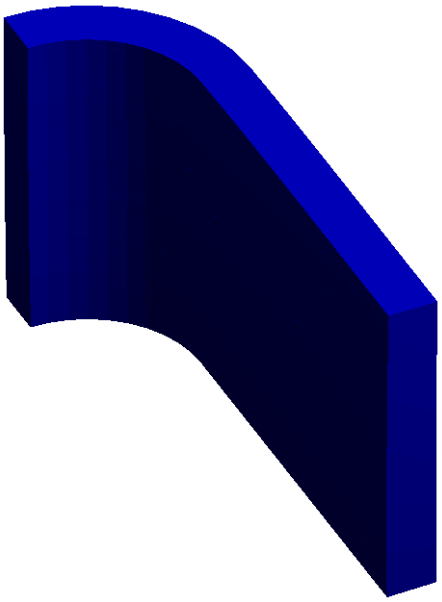

Figure 6: Deformed configuration after 10 thick layers at a printing speed of 2 min/layer.

5 CONCLUSIONS

From the purely mechanical point of view, the fresh concrete has been described through a time-dependent incremental constitutive relation in the finite strain range. The mechanical balance is therefore adapted so as to take into account this particularity together with the important presence of the concrete self-weight.

The early age creep has been motivated by the generalized Maxwell model written in rate form. Among others, only two parameters are introduced in addition to the incremental equilibrium elasticity: a characteristic time τ, and an adimensional factor f representing the amplitude of the over-stress with respect to the equilibrium incremental elasticity. For this latter, use has been made of a Saint-Venant-like model.

Numerical examples have shown the efficiency of the whole procedure. In particular, eventual structural buckling can be captured, and hence circumvented in real tests. This feature could certainly help the optimization of the printing process through simulations that could limit the number of costly real experiments.

A future step would be the identification of the mechanical parameter. In particular, we have shown through numerical simulations that the very popular slump-test could be used for this task.

REFERENCES

[1] Z. Awada and B. Nedjar. On a finite strain modeling of growth in budding yeast. *International Journal for Numerical Methods in Biomedical Engineering*, **39**(6), doi.org/10.1002/cnm.3710:e3710, 2023.

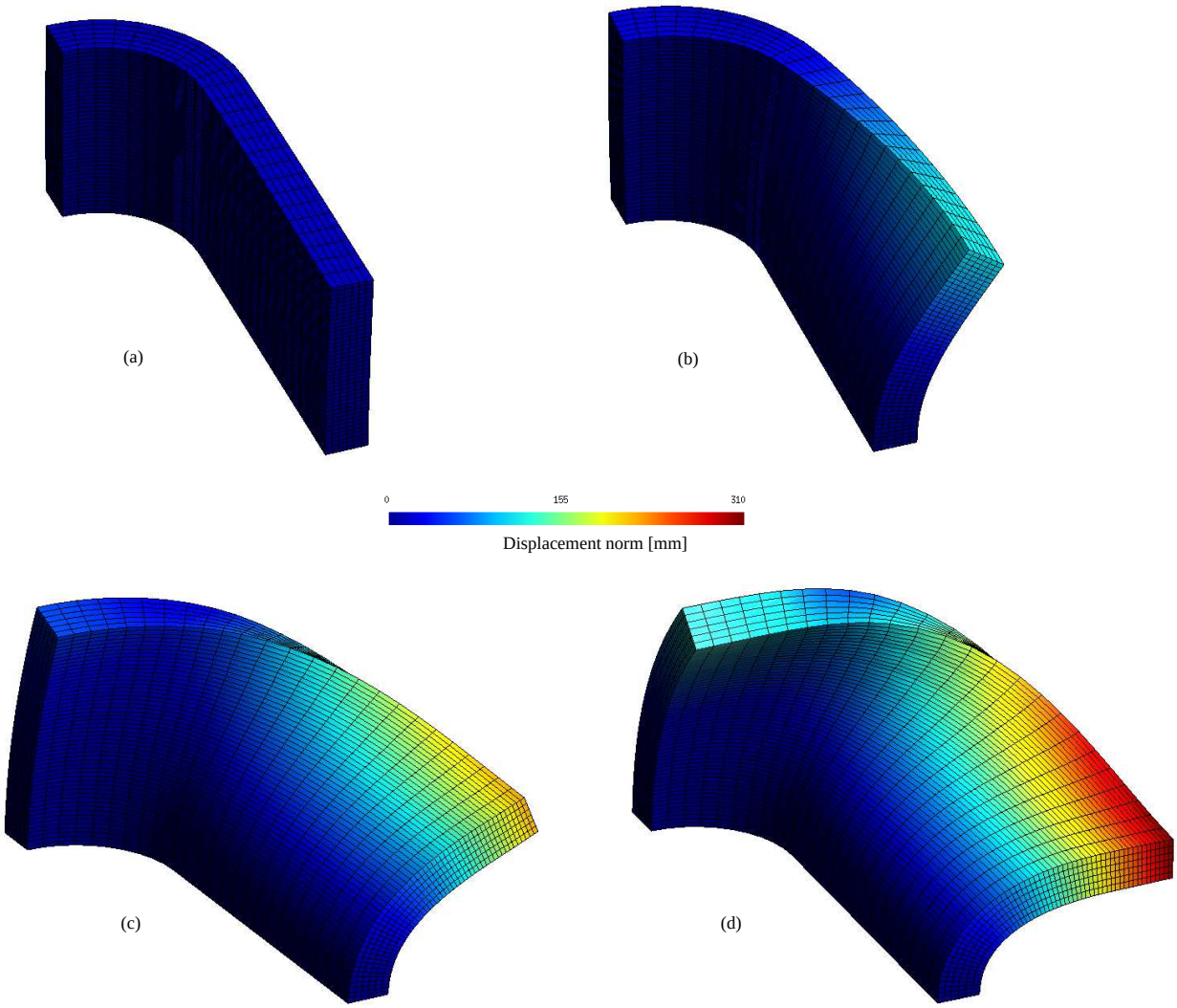

Figure 7: Deformed configurations with thick layers at a printing speed of 0.5 min/layer: (a) after 7 layers, (b) after 8 layers, (c) after 9 layers, and (d) after 10 layers.

[2] Z. P. Bažant and ed. *Mathematical modeling of creep and shrinkage of concrete*. Wiley, New York, 1988.

[3] F. Craveiro, J. P. Duarte, H. Bartolo, and P. J. Bartolo. Additive manufacturing as an enabling technology for digital construction: A perspective on construction 4.0. *Automation in Construction*, **103**:251–267, 2019.

[4] G. De Schutter and L. Taerwe. Degree of hydration based description of mechanical properties of early-age concrete. *Materials and Structures*, **29**:335–344, 1996.

[5] A. B. Hauggaard, L. Damkilde, and P. F. Hansen. Transitional thermal creep of early age concrete. *Journal of Engineering Mechanics*, **125**:458–465, 1999.

[6] M. Kaliske and H. Rothert. Formulation and implementation of three-dimensional viscoelasticity at small and finite strains. *Computational Mechanics*, **19**:228–239, 1997.

[7] J. Kruger, S. Zeranka, and G. van Zijl. 3D concrete printing: A lower bound analytical model for buildability performance quantification. *Automation in Construction*, **106**:102904, 2019.

[8] N. Labonnote, A. Ronnquist, B. Manum, and P. Rüther. Additive construction: state-of-the-art, challenges and opportunities. *Automation in Construction*, **72**(3):347–366, 2016.

[9] S. Lim, R. A. Buswell, T. T. Le, S. A. Austin, A. F. G. Gibb, and T. Thorpe. Developments in construction-scale additive manufacturing processes. *Automation in Construction*, **21**:262–268, 2012.

[10] S. A. O. Nair, H. Alghamdi, A. Arora, I. Mehdipour, G. Sant, and N. Neithalath. Linking fresh paste microstructure, rheology and extrusion characteristics of cementitious binders for 3D printing. *Journal of the American Ceramic Society*, **102**:3951–3964, 2019.

[11] B. Nedjar. On finite strain poroplasticity with reversible and irreversible porosity laws. Formulation and computational aspects. *Mechanics of Materials*, **68**:237–252, 2014.

[12] B. Nedjar. On a geometrically nonlinear incremental formulation for the modeling of 3D concrete printing. *Mechanics Research Communications*, **116**:103748, 2021.

[13] B. Nedjar. Incremental viscoelasticity at finite strains for the modelling of 3D concrete printing. *Computational Mechanics*, **69**:233–243, 2022.

[14] B. Nedjar and Z. Awada. Incremental formulation of early age concrete in the finite strain range for the modelling of 3D concrete printing. In P. Rossi and J.L. Tailhan, editors, *Numerical Modeling Strategies for Sustainable Concrete Structures, SSCS 2022, RILEM Bookseries, vol. 38*, pages 258–267. Springer, Cham, 2023.

[15] B. Panda, J. H. Lim, and M. J. Tan. Mechanical properties and deformation behaviour of early age concrete in the context of digital construction. *Composites Part B*, **165**:563–571, 2019.

[16] J. Reinold, V. Gudzulic, and Meschke G. Fiber orientation modeling exrrusion-based 3D-concrete-printing. In G. Meschke, B. Pichler, and J.G. Rots, editors, *Computational Modelling of Concrete and Concrete Structures, EURO-C 2022*, pages 202–211. Taylor & Francis, 2022.

[17] J. Reinold, V. N. Nerella, V. Mechtcherine, and Meschke G. Extrusion process simulation and layer shape prediction during 3D-concrete printing using Particle Finite Element Method. *Automation in Construction*, **136**:104173, 2022.

[18] M. P. Serdeczny, R. Comminal, D. B. Pedersen, and J. Spangenberg. Experimental validation of a numerical model for the strand shape in material extrusion additive manufacturing. *Additive Manufacturing*, **24**:145–153, 2018.

[19] J. C. Simo and T. J. R. Hughes. *Computational Inelasticity*. Springer-Verlag, New York, 1998.

[20] R. J. M. Wolfs, F. P. Bos, and T. A. M Salet. Triaxial comression testing on early age concrete for numerical analysis of 3D concrete printing. *Cement and Concrete Composites*, **104**:103344, 2019.

[21] P. Wriggers. *Nonlinear Finite Element Methods*. Springer-Verlag, Berlin, Heidelberg, 2008.

[22] J. Zhang, J. Wang, S. Dong, and B. Han. A review of the current progress and application of 3D printed concrete. *Composites Part A*, **125**:105533, 2019.